J Inorg Organomet Polym (2016) 26:190–196
DOI 10.1007/s10904-015-0296-0

Temperature and Frequency Dependence on Electrical Properties of Fe_3O_4@ Caffeic Acid Nanocomposite

A. Baykal[1] · H. Erdemi[2] · Md. Amir[1]

Received: 25 August 2015 / Accepted: 9 October 2015 / Published online: 13 October 2015

Abstract This study reports the refflux synthesis and dielectrical characterization of caffeic acid coated magnetite (Fe_3O_4) nanoparticles. Rietveld refinement confirmed the single phase product formation with the average crystallite size of 11.4 nm by Scherrer Formula. The coating of caffeic acid on the surface Fe_3O_4 nanoparticles was monitored by Fourier transform infrared spectroscopy, the interaction being via bridging oxygens of the carboxylate and the nanoparticle surface. ac/dc conductivity and dielectric analyses of product revealed semiconductor characteristics varying with temperature. ac conductivity increases regularly with temperature and do not show frequency-dependent behavior particularly at lower frequency regime whereas it exhibits a significant temperature dependent behavior at medium frequencies and at higher temperatures.

Keywords Fe_3O_4 · Caffeic acid · Conductivity · Dielectric properties · Spinel compounds

1 Introduction

Magnetic polymer nanocomposites (which contain both organic and inorganic part) are important class of functional materials, in which the magnetic nanoparticles are embedded in nonmagnetic matrix. Polymer coatings can enhance compatibility with organic ingredients, reduce susceptibility to leaching and protect particle surfaces from oxidation (improves dispersion qualities, chemical stability and may reduce toxicity) [1, 2]. In last two decades, the scientific and technological importance (interest) of polymer–inorganic nanocomposites (PINCs) is getting increase because the incorporation of inorganic nanoparticles into the polymer matrix can provide high-performance novel materials that can find applications in many industrial fields [3, 4]. These magnetic nanocomposites can be used as drug targeting, electromagnetic devices (electromagnetic wave absorption), bio-separation and etc [5, 6].

Among the magnetic nanomaterials doped into the polymer matrix, ferrites (Fe_3O_4, $CoFe_2O_4$, $NiFe_2O_4$) are being used so much due to intrinsic magnetic and dielectric properties [7–13].

Caffeic acid is an organic compound that is classified as hydroxycinnamic acid and it is is a well known natural aromatic compound derived from the phenyl propanoid pathway in plants [14].

In this study, caffeic acid coated Fe_3O_4 nanocomposite were synthesized by reflux method and the effect of caffiec acid coating structural and dielectric properties of Fe_3O_4 was studied.

2 Experimental

2.1 Chemicals

$FeCl_3{\cdot}6H_2O$, $FeCl_2{\cdot}4H_2O$, caffeic acid ($C_9H_8O_4$, CA) and NaOH were sourced from Merck and were used without further purification.

✉ A. Baykal
hbaykal@fatih.edu.tr

[1] Department of Chemistry, Fatih University, Büyükçekmece, 34500 Istanbul, Turkey

[2] Department of Polymer Engineering, Yalova University, 77100 Yalova, Turkey

2.2 Instrumentations

X-ray powder diffraction (XRD) analysis was conducted on a Rigaku Smart Lab operated at 40 kV and 35 mA using Cu Kα radiation ($\lambda = 1.54059$ Å).

Fourier transform infrared (FT-IR) spectra of the samples were recorded with a Perkin–Elmer BX FT-IR infrared spectrometer in the range 4000–400 cm^{-1}.

Scanning electron microscopy (SEM) analysis was performed, in order to investigate the microstructure of the sample, using FEI XL40 Sirion FEG digital scanning microscope. Samples were coated with gold at 10 mA for 2 min prior to SEM analysis.

The thermal stability was determined by thermogravimetric analysis (TGA, Perkin–Elmer Instruments model, STA 6000). The TGA thermograms were recorded for 5 mg of powder sample at a heating rate of 10 °C/min, over the temperature range 30–750 °C under a nitrogen atmosphere.

The real (ε′) and imaginary (ε″) parts of complex dielectric permittivity e*[= ε′(ω) + ε″(ω)] were measured with a Novocontrol dielectric-impedance analyzer. The dielectric data (ε′, ε″) were collected as a function of temperature and frequency. These films were sandwiched between gold blocking electrodes and the conductivities were measured in the frequency range of 0.1 Hz to 3 MHz at 10 °C intervals. The temperature change was controlled with a Novocontrol cryosystem with a precision of 0.01 °C.

2.3 Synthesis of Fe_3O_4@CA Nanocomposite

The detailed synthesis of the product was given in our previous publication [15]. The stoichiometric amount of iron chloride salts ($FeCl_3 \cdot 6H_2O$ and $FeCl_2 \cdot 4H_2O$) (according to the molar raito of $Fe^{3+}/Fe^{2+} = 2$) were dissolved in deionized water with continuous stirring. Then certain amount of CA was added and pH of the solution was arranged to 8 by using 1.5 M NaOH by dropwise then refluxed at 80 °C for 5 h. Whole experiment was done under Ar gas and on magnetic stirrer. Finally, product was cooled to RT, washed with ethanol–water solution and dried at 70 °C for 4 h.

3 Results and Discussion

3.1 FT-IR Analysis

FT-IR spectra of CA and Fe_3O_4@CA nanocomposite are presented in Fig. 1a, b respectively. Three characteristic peaks in CA FT-IR spectrum (Fig. 1a) correspond to the C=O stretching of free carboxylic acids at 1607 cm^{-1} and symmetric COO^- stretching at 1430 cm^{-1} [15, 16].

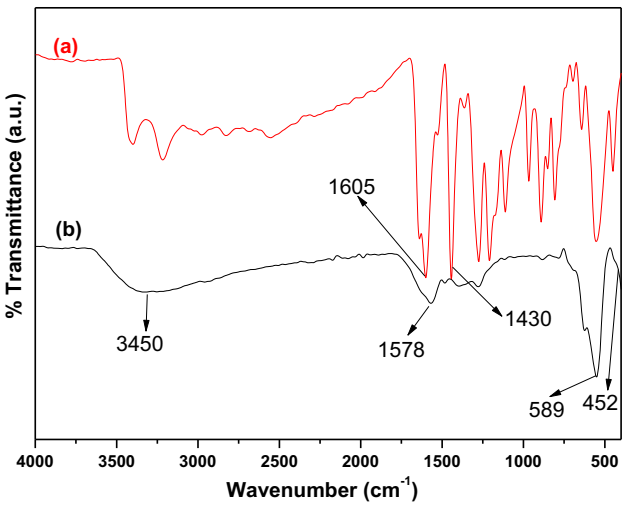

Fig. 1 FT-IR spectra of **a** CA and **b** Fe_3O_4@CA nanocomposite

Whereas the 1605 cm^{-1} peak assignable to the C=O vibration (symmetric stretching) from the COOH group of CA shifts to an intense band at about 1578 cm^{-1} for the Fe_3O_4@CA nanocomposite (Fig. 1b) revealing the binding of a CA to the magnetite surface [17–21]. A large and intense band at 3450 cm^{-1} that could be assigned to the structural OH groups as well as to the traces of molecular water. Two sharp bands at 2924 and 2854 cm^{-1} were attributed to asymmetric and symmetric CH_2 stretching vibrations, respectively. Additionally, Figs. 1b and 3 shows metal–oxygen band, v_1, at 589 cm^{-1} corresponding to intrinsic streching vibrations of the metal at tetrahedral site (M_{tetra}-O) whereas metal–oxygen band at 452 cm^{-1}, v_2, is assigned to octahedral–metal stretching (M_{octa}-O) [11, 22–26].

3.2 XRD Analysis

The XRD powder pattern and Rietveld refinement result of Fe_3O_4@CA nanocomposite are depicted in Fig. 2 which reveals that CA coating does not result in the phase change of bare Fe_3O_4. All of the observed diffraction peaks [(111), (220), (311), (222), (400), (422), (511), (440)], were indexed by the inverse spinel cubic structure (JCPDS no. 99-100-2409) and no impurity was detected. Scherrer equation was used for the calculation of crystallite size (D_{XRD}) and found as 11.4 nm [15].

3.3 TG Analysis

The TG curves of CA and Fe_3O_4@CA nanocomposite are presented in Fig. 3. As it can be seen from Fig. 1 a, Pure caffeic acid started to decompose at 100 °C and decomposition was completed at ~200 °C (Fig. 3a). For the

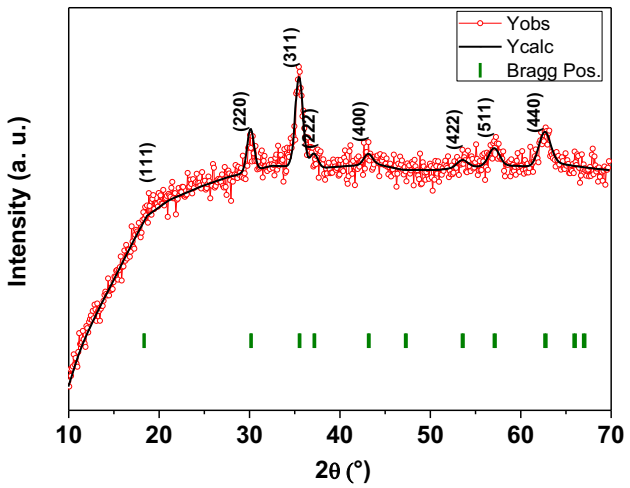

Fig. 2 XRD profile matching of Fe_3O_4@CA nanocomposite

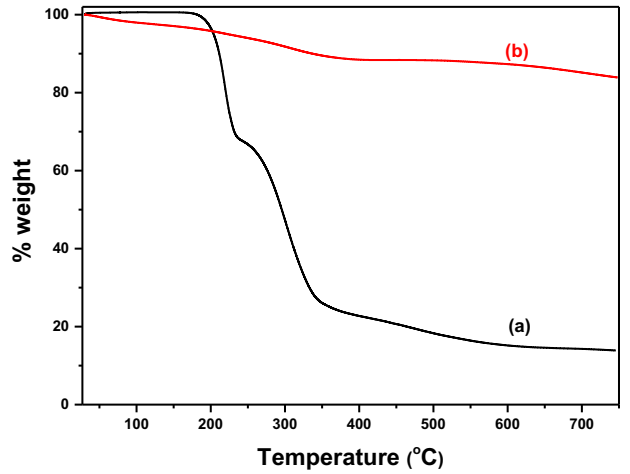

Fig. 3 TG thermograms of **a** CA and **b** Fe_3O_4@CA nanocomposite

nanocomposite a weight loss of ~1 wt% was observed between room temperature and 200 °C, which is attributed to the evaporation of physisorbed water and loosely coordinated water in the interlayer. Then sharp weight loss was observed upto 750 °C which was due to the decomposition then evaporation of CA. Upto this temperature, inorganic phase (Fe_3O_4) is still present. These TG observation was revealed that the percentage of organic to inorganic content in the product is 16 and 84 respectively [15].

3.4 SEM–EDX Analysis

The SEM micrograph and EDX spectra of Fe_3O_4@CA nanocomposite are given in Fig. 4a, b respectively. As it was given in Fig. 4a, product appears the uniform sphere-like shape with smooth surface which has the estimated particle size of 14 nm. EDX result confirmed the absence of impurity and the expected chemical formula (Fig. 4b).

3.5 Electrical Properties

3.5.1 ac Conductivity

The variation of ac conductivity, $\sigma_{ac}(\omega)$, of Fe_3O_4@CA nanocomposite was measured in the temperature range of 20–120 °C and frequency range of 1 Hz–1 MHz using impedance spectroscopy and results are displayed in Fig. 5. The frequency dependent $\sigma_{ac}(\omega)$, was obtained using following Eq. [1]:

$$\sigma'(\omega) = \sigma_{ac}(\omega) = \varepsilon''(\omega)\omega\varepsilon_0 \quad (1)$$

where $\sigma'(\omega)$ is the real part of conductivity, ω (= $2\pi f$) is the angular frequency, ε" is the imaginary part of complex dielectric permittivity (ε^*) and $\varepsilon 0$(= $8.852 \times 10 - 14$ F cm^{-1}) is the vacuum permittivity.

The frequency dependent ac conductivity curves show similar behavior at all temperatures in the log–log plot. The frequency dependent linear increases in low frequency regime at low temperatures is due to the blocking electrode polarizations. The curves of ac conductivity versus frequency involve well-developed conductivity plateau regions particularly at low frequencies while the conductivity plateaus shift and broaden towards higher frequencies as temperature increases. The ac conductivity increases regularly with temperature and do not show frequency-dependent behavior particularly at lower frequency regime whereas it exhibits a significant temperature dependent behavior at medium frequencies and at higher temperatures. The σ_{ac} increases regularly with a nearly equivalent slope as temperature increases and this increase is more distinct and distinguishable above a phase transition temperature of about 80 °C. The ac conductivity increased from 4.27×10^{-8} to 4.78×10^{-8} as temperature raised from 70 to 80 °C at 100 Hz, while the conductivity enhanced from 6.69×10^{-8} to 1.07×10^{-7} as temperature increased from 90 to 100 °C at same frequency. Such a considerable enhancement in ac conductivity over phase transition temperature may be due to the contribution of ionic conductivity [19, 27]. At elevated temperatures, the mobility of charge carriers increases due to the influence of the local dynamics and percolation of the nanocomposites.

Firstly, Fe_3O_4@CA nanocomposite can form a random network at low temperatures. As the temperature increases regularly, the nanoparticles develop more organized structure and display more capacitive behavior and weak frequency response on hopping conduction which gives rise to an increment in electrical conductivity. Additionally, the interaction of Fe_3O_4 nanoparticles may also increase with the applied temperature leading a percolated path so that electrical current can flow through both semiconducting Fe_3O_4 nanoparticles and caffeic acid as reported previously [28–31]. This temperature-assisted

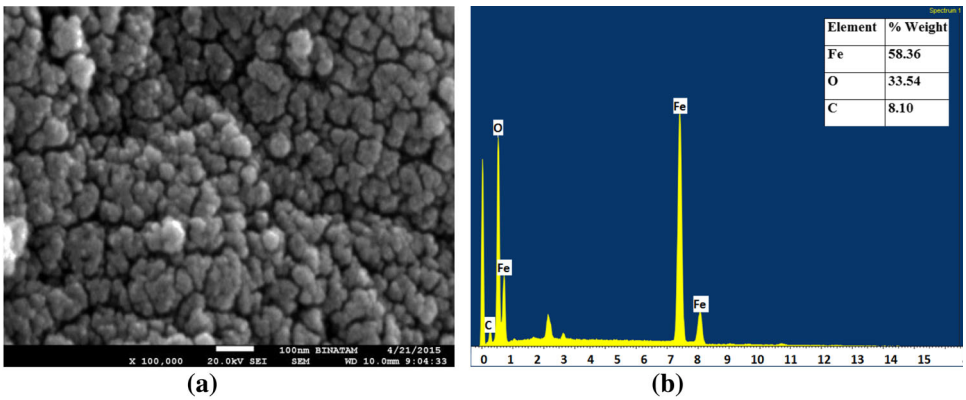

Fig. 4 **a** SEM micrograph and **b** EDX spectra of Fe_3O_4@CA nanocomposite

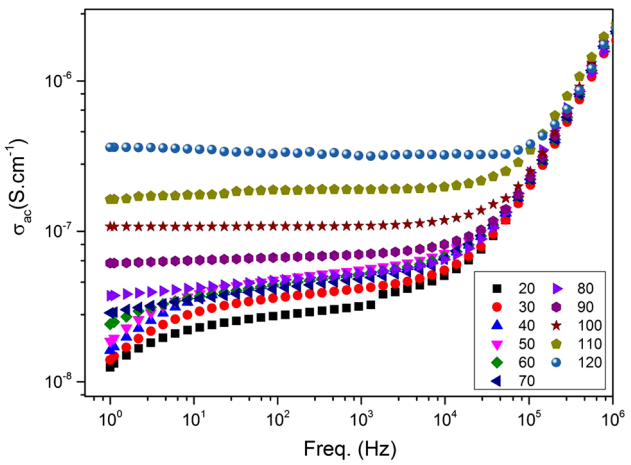

Fig. 5 The variation of ac conductivity of Fe_3O_4@CA nanocomposite as a function of frequency and temperature

phenomenon based on formation of the organized X-coated magnetite NPs which induces variation of overall conductivities with temperatures.

Random magnetite distribution in the nanocomposite determines the low and high frequency response, as a result substantial variation in distribution of nanocomposite was observed. As a result of this the conductivity of the nanocomposite increases constantly with frequency in the presence of a percolated path of CA across the nanocomposite resulting growth of well-defined plateaus over a certain temperatures. The reorganization of the Fe_3O_4@CA nanocomposite is completed over 80 °C. Subsequently, the ac conductivity increases regularly with reciprocal temperature in Arrhenius plot up to 80 °C, and then a transition takes place. The conductivity kept on rising with a sharp increment in slope with reciprocal temperature over 80 °C which is basically due to the effect of the thermal energy applied on Fe_3O_4@CA nanocomposite. The conductivity of naked Fe_3O_4 NPs is higher as compared with Fe_3O_4@CA nanocomposite revealing the fact that the surface bonding between Fe_3O_4 NPs and CA may decrease the free surface charge in the medium which results in a reduction in conductivity [16, 28].

3.5.2 *dc Conductivity*

The low frequency-independent plateaus in ac conductivity curve describing the electrode–electrolyte interface phenomena is ascribed to the space charge polarization at the blocking electrode and is related to the dc conductivity (σ_{dc}). The dc conductivity values were acquired by linear fittings of well-developed plateau regions to zero frequency in log σ_{ac} versus log f plot. Figure 6. represents the variation of log σ_{dc} with the inverse of absolute temperature of naked Fe_3O_4 NPs and Fe_3O_4@CA nanocomposite.

The dc conductivity curves exhibit significant temperature-dependent behavior and can be classified into three regions over the range of 20–120 °C. The temperature-dependent dc conductivity can be interpreted according to the following Arrhenius equation:

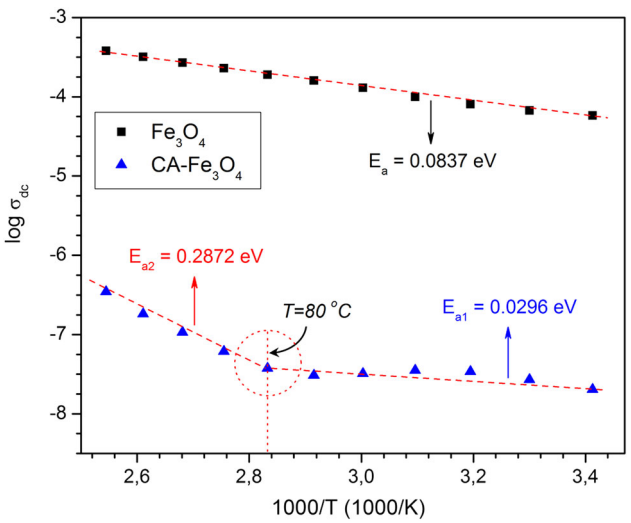

Fig. 6 The variation of dc conductivity of Fe_3O_4 NPs and Fe_3O_4@CA nanocomposite with reciprocal temperature

$$\log \sigma = \log \sigma_0 - \frac{E_a}{kT} \quad (2)$$

where σ_{dc} is the dc conductivity, σ_0 is the pre-exponential term, E_a is the activation energy, k is the Boltzmann constant (8.617×10^{-5} eV K^{-1}) and T is the absolute temperature.

The dc conductivity of magnetite increases linearly with temperature displaying no transition and possessing only single activation energy while Fe_3O_4@CA nanocomposite displays a sudden incline in conductivity with temperature over 80 °C corresponding to the transition temperature. The dc conductivity of Fe_3O_4@CA nanocomposite demonstrates two values of the activation energies before and after transition temperature. It is obvious that this transition above 80 °C can be assigned to the magnetic transformation of Fe_3O_4-NPs as discussed in literature [32]. It was reported that magnetic transformation of the single crystals of iron oxide takes place in the temperature range of 70–190 °C. It has been shown that the main conduction in magnetite nanocomposites is due to hopping process based on Verwey de Boer mechanism [33]. The electron exchange occurs between the ions of the same elements existing in more than one valence state and distributed over crystallographic lattice sites which provides low mobility systems similar to ferrites. With temperature the drift mobility of charge carriers increases followed by an improvement in dc conductivity [34, 35]. The activation energies, E_a, were calculated from the slopes of Arrhenius plots before (20–80 °C) and after (80–120 °C) transition region, and E_a values were found to be $E_{a1} = 0.0296$ eV, $E_{a2} = 0.2872$ eV which is in good agreement with the previously reported similar works [16, 36].

3.5.3 *Dielectric Permittivity*

The variation of the dielectric constant (ε′) and dielectric loss (ε″) Fe_3O_4@CA nanocomposite as a function of frequency and temperature are shown in Figs. 7 and 8 respectively. It can be seen that dielectric constant (ε′) show strong frequency dependence as well as temperature dependence. It is clear that the dielectric constant and dielectric loss decreases with increasing frequency.

The dielectric constants, in general, decline exponentially with frequency. The inset displays the variation of dielectric constants with higher frequencies (>10^2 Hz). The decrease is rather significant particularly at low temperatures and at low frequency region while it exhibits relatively slight decline at elevated temperatures and it becomes comparable at high frequencies (Fig. 7). The result can be described as a complete reorganization of nanocomposite at high temperature range and phase transition while passing through the medium temperature range

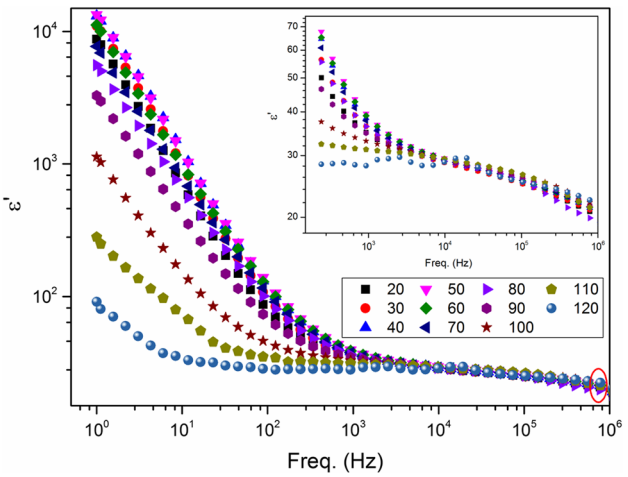

Fig. 7 The variation of the dielectric constant at different temperatures as a function of frequency for Fe_3O_4@CA nanocomposite

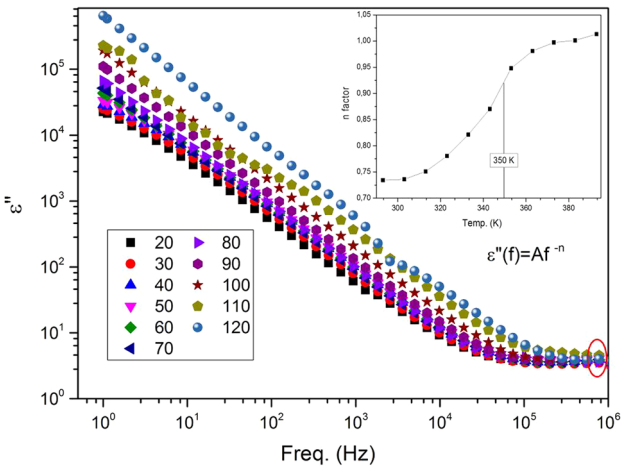

Fig. 8 The variation of the dielectric loss at different temperatures as a function of frequency for Fe_3O_4@CA nanocomposite with inset for n factors

resulting from the relaxation of CA molecules. The dielectric constant decreases regularly with frequency and then reaches a nearly constant value due to the fact that beyond a certain frequency the electron exchange between the vacant sites cannot follow the applied external field particularly at high temperatures.

The high values of dielectric constants at lower frequency region is essentially due to material electrode interface polarization processes for the inhomogeneous double layer dielectric structure [37, 38]. The frequency-dependent dielectric dispersion curves of such inhomogeneous systems can be described by Koop's theory based on the Maxwell–Wagner model [38–40]. The inhomogeneous dielectric structure including two layers with dissimilar dielectric constants. The first one is the highly conducting large ferrite grains separated by the second thin layer of the

moderately poor conducting grain boundaries. The grain boundaries are more effective at lower frequencies while grains are more effective at higher frequencies [41–43]. The conductivity difference between grains and grain boundaries lead to the accumulation of charge carriers in separated boundaries and an enhancement in dielectric constants.

It was observed that dielectric constant increases with temperature up to about 70 °C due to the development of interfaces between CA and Fe_3O_4 NPs as reported in literature [6]. Subsequently, transition region takes place as a consequence ε′ switches to decline substantially at higher temperatures (>80 °C) which is in very good agreement with previously reported works [16, 44].

Figure 8 displays the variation of the dielectric loss with frequency at various temperatures which can be analytically well characterized by power laws ($\varepsilon''(f) = Af^{-n}$). The variation of the exponent "n" with temperature as inset in Fig. 8. The related power law exponents are in the range of 0.73–1.01 which is in agreement with the values reported in literature [45]. The studied characteristic nature of Fe_3O_4@CA nanocomposite seems to be comparable to that of its conductivity as presented in earlier studies and the inset is given for comparison [16, 28]. The dielectric loss, generally, exhibits a sharp linear decrease in low and medium frequency regions whereas the variation is rather small or it stays almost constant at higher frequencies.

It is obvious that dielectric loss increases with increase in temperature and the increment is higher over transition temperature of 80 °C. On the other hand, the exponent "n" displays a nearly linear increase with temperature up to 80 °C and then it keeps on rising with significant changes in slope at elevated temperatures which is due to the reorganization of nanocomposite at a given temperature boundary.

The temperature-dependency of "n" values for Fe_3O_4@CA nanocomposite suggests thermally activated polarization mechanism. The thermal energy increases the mobility and concentration of the charge carriers. Accordingly, the interface polarization is significant at lower frequencies while other mechanisms such as electronic and ionic considerable at higher frequencies [46, 47].

3.5.4 Dielectric Loss Tangent (tan δ)

The variation of the dielectric-loss tangent (tan δ) with temperature is given in Fig. 9. As a common trend, the dielectric-loss tangent does not varies remarkably until phase transition temperate of 80 °C while a considerable enhancement was observed at higher temperatures for all frequencies. The polarization effect is used to explain the

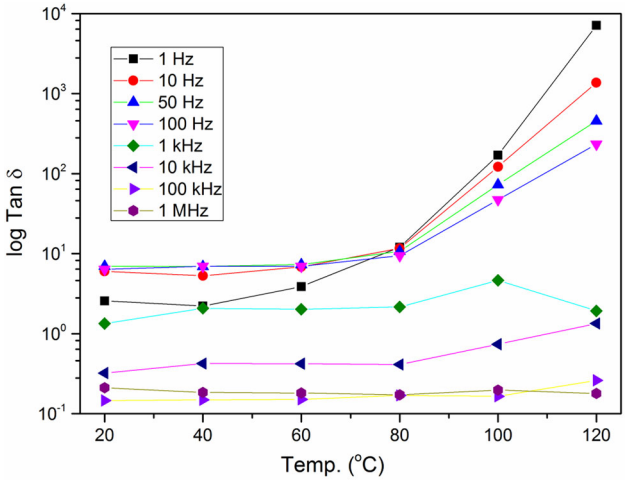

Fig. 9 The log tan δ (dissipation factor) of Fe_3O_4@CA nanocomposite versus temperature at different frequencies

temperature-dependent behavior of the dielectric-loss tangent. With temperature, the electrical conductivity increases due to the thermal process and mobility of the electrical charge carriers. Accordingly, the dielectric polarization increases leading to an increase in the dielectric constant and dielectric loss tangent. Additionally, the dielectric loss tangent reaches a maximum at a certain frequency which broadens and shifts towards higher frequencies with applied frequency and temperature. This characteristic feature may be assigned to self-alignment of the dipoles with the alternating fields as discussed [48].

4 Conclusion

Fe_3O_4@CA nanocomposite was successfully synthesized by reflux synthesis route. The structural, spectroscopic, morphological and electrical analyses were done XRD, FT-IR, SEM and impedans spectroscopy. FT-IR analysis confirmed the capping of CA on the surface of Fe_3O_4 nanoparticles. As the temperature increases regularly, the nanoparticles develop more organized structure and display more capacitive behavior and weak frequency response on hopping conduction which gives rise to an increment in electrical conductivity. It can be seen that dielectric constant (ε′) show strong frequency dependence as well as temperature dependence. It is clear that the dielectric constant and dielectric loss decreases with increasing frequency.

Acknowledgments Md.Amir is also a thanks to the Turkish Research Council for his master studies and for Foreing students scholarship program of 2215.

References

1. H. Deligöz, A. Baykal, M. Şenel, H. Sözeri, E. Karaoğlu, M.S. Toprak, Synth. Met. **162**, 590–597 (2012)
2. L. Udrea, D. Hritcu, M. Popa, O. Rotariu, J. Magn. Magn. Mater. **323**, 7–13 (2011)
3. S. Li, M.M. Lin, M.S. Toprak, D.K. Kim, M. Muhammed, Nano Rev. **1**, 5214–5220 (2010)
4. Y. Li, G. Chen, Q. Li, G. Qiu, X. Liu, J. Alloy. Compd. **509**, 4104–4110 (2011)
5. A. Dey, S. De, A. De, S.K. De, Nanotechnology **15**, 1277–1285 (2004)
6. D. Ding, X. Yan, X. Zhang, Q. He, B. Qiu, D. Jiang, H. Wei, J. Guo, A. Umar, L. Sun, Q. Wang, M.A. Khan, D.P. Young, X. Zhang, B. Weeks, T.C. Ho, Z. Guo, S. Wei, Superlattices Microstruct. **85**, 305–320 (2015)
7. Md Amir, B. Ünal, E. Sagar, M. Shirsath, M. Geleri, M. Sertkol, A. Baykal, Superlattices Microstruct. **85**, 747–760 (2015)
8. M. Aydın, B. Ünal, B. Esat, A. Baykal, E. Karaoglu, M.S. Toprak, H. Sözeri, J. Alloy. Compd. **514**, 45–53 (2012)
9. Z. Durmus, H. Sözeri, B. Unal, A. Baykal, R. Topkaya, S. Kazan, M.S. Toprak, Polyhedron **30**, 322–328 (2011)
10. S. Bahceci, B. Unal, A. Baykal, H. Sözeri, E. Karaoglu, B. Esat, J. Alloy. Compd. **509**, 8825–8831 (2011)
11. M. Günay, H. Erdemi, A. Baykal, H. Sözeri, M.S. Toprak, Mater. Res. Bull. **48**, 1057–1064 (2013)
12. M. Khairy, Synth. Met. **189**, 34–41 (2014)
13. N. Gandhi, K. Singh, A. Ohlan, D.P. Singh, S.K. Dhawan, Compos. Sci. Technol. **71**, 1754–1760 (2011)
14. N.R. Prasad, A. Karthikeyan, S. Karthikeyan, B.V. Reddy, Mol. Cell. Biochem. **349**, 11–19 (2011)
15. A. Baykal, Md Amir, S. Güner, H. Sözeri, J. Magn, Magn. Mater. **395**, 199–204 (2015)
16. H. Erdemi, A. Baykal, E. Karaoğlu, M.S. Toprak, Mater. Res. Bull. **47**, 2193–2199 (2012)
17. D. Maity, D. Agrawal, J. Magn. Magn. Mater. **308**, 46–55 (2007)
18. H. Cui, D. Li, Z. Zhang, Mater. Lett. **143**, 38–40 (2015)
19. B. Unal, Z. Durmuş, H. Kavas, A. Baykal, M.S. Toprak, Mater. Chem. Phys. **123**, 184–190 (2010)
20. E. Karaoglu, A. Baykal, H. Deligöz, M. Şenel, H. Sözeri, M.S. Toprak, J. Alloy. Compd. **509**, 8460–8468 (2011)
21. M. Gunay, H. Kavas, A. Baykal, Mater. Res. Bull. **48**, 1296–1303 (2013)
22. Z. Durmus, H. Kavas, A. Baykal, H. Sozeri, L. Alpsoy, S.Ü. Çelik, M.S. Toprak, J. Alloy. Compd. **509**, 2555–2561 (2011)
23. M. Aydın, Z. Durmus, H. Kavas, B. Esat, H. Sözeri, A. Baykal, F. Yılmaz, M.S. Toprak, Polyhedron **30**, 1120–1126 (2011)
24. R.D. Waldron, Phys. Rev. **99**, 1727–1735 (1955)
25. K. Chinnaraj, A. Manikandan, P. Ramu, S.A. Antony, P. Neeraja, J. Supercond. Novel Magn. **28**, 179–190 (2015)
26. A. Manikandan, J.J. Vijaya, J.A. Mary, L.J. Kennedy, A. Dinesh, J. Ind. Eng. Chem. **20**, 2077–2085 (2014)
27. A. Baykal, N. Bıtrak, B. Ünal, H. Kavas, Z. Durmus, Ş. Özden, M.S. Toprak, J. Alloy. Compd. **502**, 199–206 (2010)
28. E. Temizel, E. Ayan, M. Şenel, H. Erdemi, M.S. Yavuz, H. Kavas, A. Baykal, R. Öztürk, Mater. Chem. Phys. **131**, 284–291 (2011)
29. E. Karaoğlu, A. Baykal, H. Erdemi, L. Alpsoy, H. Sozeri, J. Alloy. Compd. **509**, 9218–9225 (2011)
30. H. Deligöz, E.E. Tanrıverdi, Z. Durmus, M.S. Toprak, Mater. Res. Bull. **47**, 537–543 (2012)
31. S. Bhattacharyya, S.K. Saha, D. Chakravorty, J. Polym. Sci. **38**, 1193–1200 (2000)
32. H. Watanabe, N. Tsuya, Phys. Chem. Metall. Ser. A **2**, 29–36 (1950)
33. E.J. Verwey, J.H. de Boer, Rec. Trans. Chim. Phys. Bas. **55**, 531–538 (1936)
34. E.J.W. Verway, P.W. Haayman, Physica **8**, 979–985 (1941)
35. V.L.G. Uitert, Proc. IRE **44**, 1294–1299 (1956)
36. Z. Durmus, H. Erdemi, A. Aslan, M.S. Toprak, H. Sozeri, A. Baykal, Polyhedron **30**, 419–426 (2011)
37. S. Ukishima, M. Iijima, M. Sato, Y. Takahashi, E. Fukada, Thin Solid Films **308–309**, 475–479 (1997)
38. J.A. Maxwell, *Treatise on Electricity and Magnetism* (Clarendon Press, Oxford, 1982)
39. K.W. Wagner, Ann. Phys. **345**, 817–855 (1913)
40. C.G. Koops, Phys. Rev. **83**, 121–124 (1951)
41. K.M. Batoo, S. Kumar, C.G. Lee, Alimuddin. Curr. Appl. Phys. **9**, 1397–1406 (2009)
42. M. Manjurul Haquea, M. Huqa, M.A. Hakim, Mater. Chem. Phys. **112**, 580–586 (2008)
43. B. Ünal, Z. Durmus, A. Baykal, H. Sözeri, M.S. Toprak, L. Alpsoy, J. Alloy. Compd. **505**, 172–177 (2010)
44. S.M. Patange, S.E. Shirsath, K.S. Lohar, S.S. Jadhav, N. Kulkarni, K.M. Jadhav, Physica B: Cond. Matter **406**, 663–668 (2011)
45. M. Wan, J. Fan, Polym. Sci. Part A. Polym. Chem. **36**, 2749–2756 (1998)
46. D.J. Griffiths, *Introduction to Electrodynamics* (Prentice Hall, Upper Saddle River, 1999)
47. J.D. Jackson, *Classical Electrodynamics* (Wiley, New York, 1999)
48. D.G. Chen, X.G. Tang, J.J. Tong, J.B. Wu, Y.P. Jiang, Q.X. Liu, Solid State Commun. **151**, 1042–1048 (2011)